Angle-resolved study of resonant Auger decay and fluorescence emission processes after core excitations of the terminal and central nitrogen atoms in N_2O

A. Knie,[1,*] M. Ilchen,[2,3] Ph. Schmidt,[1] Ph. Reiß,[1] C. Ozga,[1] B. Kambs,[1] A. Hans,[1] N. Müglich,[1] S. A. Galitskiy,[1] L. Glaser,[2] P. Walter,[2] J. Viefhaus,[2] A. Ehresmann,[1] and Ph. V. Demekhin[1,†]

[1]*Institut für Physik, Universität Kassel, Heinrich-Plett-Strasse 40, 34132 Kassel, Germany*

[2]*Deutsches Elektronen-Synchrotron DESY, Notkestraße 85, 22607 Hamburg, Germany*

[3]*European XFEL GmbH, Albert-Einstein-Ring 19, 22761 Hamburg, Germany*

(Received 28 May 2014; published 16 July 2014)

Angular distributions of the $N_2O^+(X)$ and $N_2O^+(A)$ photoelectrons were measured as functions of the exciting-photon energy with small bandwidth in the vicinity of the resonant $N_t(1s \to \pi^*)$, $N_t(1s \to \sigma^*)$, and $N_c(1s \to \pi^*)$ core excitations of N_2O. For selected exciting-photon energies in this range, angular distribution parameters of the $N_2O^+(A \to X)$ fluorescence were also determined. These data are interpreted by *ab initio* calculations. Long-range exciting-photon energy dependencies of the photoelectron angular distribution parameters $\beta_X^e(\omega)$ and $\beta_A^e(\omega)$, recorded vibrationally unresolved, are attributed to an electronic state interference between the direct and the different resonant amplitudes for the population of the final ionic states. In addition to that, strong influence of lifetime vibrational interference is identified in the observed dispersion of the vibrationally resolved fluorescence angular distribution parameter $\beta 2_A^X(\omega)$ across the electronic resonances.

DOI: 10.1103/PhysRevA.90.013416 PACS number(s): 33.80.Eh, 32.80.Hd, 33.50.Dq

I. INTRODUCTION

The N_2O molecule is one of the simplest prototype systems to study electronic properties of two equivalent atoms in different chemical surroundings. Particularly striking is the possibility to selectively probe core electrons localized on either the terminal or the central nitrogen atom and to compare their different deexcitation spectra. Therefore, over the last decades N_2O has attracted considerable attention from both experimental and theoretical sides and a vast literature has been published on the subject. For instance, the relatively large chemical shift of about 4 eV between the binding energies of the $N_t(1s)$ and $N_c(1s)$ core electrons is evident in x-ray photoelectron spectra of N_2O (see, e.g., recent works [1,2]). This results in the formation of two overlapping normal Auger decay spectra of the N_t and N_c K shells [3,4]. Similar chemical shifts are also evident in absorption spectra measured in the vicinity of the corresponding core excitations [5,6], and different dynamics of relaxation of the core-excited states can be seen in the corresponding resonant Auger decay [7–9] or fragmentation [10–13] spectra.

Angle resolved spectroscopy provides important complementary information on the photoinduced relaxation dynamics [14], which may not be accessible in the total (solid-angle-integrated or magic-angle-recorded) spectra [15]. This is because angular distribution parameters are very sensitive to the phases of the outgoing partial photoelectron waves and to their interference. The aforementioned advantage of the angle resolved spectroscopy has already been utilized a few times to investigate photoelectron angular distributions above N_t and N_c K-shell thresholds of N_2O [16] and to study its angle-resolved total ion-yield spectra below N_t, N_c, and O K-shell thresholds [17,18]. Here we report a joint experimental and theoretical study of the angle resolved participator resonant Auger electron spectra of the core-excited N_2O molecule complemented by the angle resolved fluorescence spectrum for the subsequent relaxation in the N_2O^+ ion. A simultaneous analysis of the data obtained for the two subsequent decays allows us to get a deeper insight into the processes.

Typically, in the vicinity of the core excitations of molecules, the resonant channel for the excitation and Auger decay of the intermediate electronic state dominates over the weak direct nonresonant photoionization. Therefore, electronic state interference (ESI [19]) between the direct and the resonant amplitudes for the population of the final ionic states is almost negligible in the total (angle-unresolved) decay spectra recorded in the on-resonance excitation regime. Here, for the closely neighboring vibronic excited states overlapping within their natural widths, lifetime vibrational interference (LVI [20]) is the dominant effect [21]. First indications of the influence of the weak direct ionization channel on the total resonant Auger decay spectra of molecules were found in the off-resonance excitation (energy detuning) regime [22–25].

In the angle resolved decay spectra of molecules, both LVI and ESI effects become much more pronounced, even for well-separated vibronic resonances exhibiting very weak LVI in the total cross sections [26], and even if ESI is strictly symmetry forbidden in the solid-angle-averaged spectra [27]. These first qualitative interpretations were fully explained by *ab initio* calculations and complementary observations in our previous works [28–31] for CO and NO molecules, and later by others [32] for O_2. It was shown in [28–31] that ESI (and especially the weak direct photoionization channel) induces broad-energy-range dispersions of the angular distribution parameters for Auger electrons and for fluorescence photons, whereas LVI gives rise to prominent variations of the angular distribution parameters across the resonances. In the present work we identify strong interference effects in the angle resolved electron-fluorescence cascade decay spectra of the core-excited N_2O molecule.

*knie@physik.uni-kassel.de
†demekhin@physik.uni-kassel.de

The paper is organized as follows. In Sec. II we briefly discuss the processes relevant for the present study. Our experimental and theoretical approaches are outlined in Secs. III and IV, respectively. The present experimental and theoretical results are compared and discussed in Sec. V. We conclude in Sec. VI with a short summary.

II. THE PROCESS

The processes under the present experimental and theoretical investigation can be schematically represented as the following cascade of decays. Linearly polarized synchrotron radiation with photon energy $\hbar\omega$ excites the ground state of N_2O into the $N_t(1s \rightarrow \pi^*)$, $N_t(1s \rightarrow \sigma^*)$, and $N_c(1s \rightarrow \pi^*)$ resonances (referred to hereafter as π_t^*, σ_t^*, and π_c^* resonances with energies of around 401.1, 403.9, and 404.7 eV [9,17], respectively),

$$1s_t^2 1s_c^2 7\sigma^2 2\pi^4 \left(X\ ^1\Sigma^+, \Omega_0\chi_0\right) + \hbar\omega \rightarrow 1s^{-1}\{\pi_t^*/\sigma_t^*/\pi_c^*\}\left(^1\Pi/\ ^1\Sigma^+/\ ^1\Pi, \Omega_r\chi_r\right), \quad (1)$$

where Ω is the projection of the total electronic angular momentum along the molecular quantization axis, which is a good quantum number for an electronic state in the linear geometry of N_2O. χ stands for the wave function for the nuclear quantum motion. The closed shells of N_2O not participating in the present process are omitted for brevity.

Below we consider the following two pathways for relaxation of the intermediate core-excited states via a participator Auger decay into the $N_2O^+(A\ ^2\Sigma^+, \Omega'\chi')$ and $N_2O^+(X\ ^2\Pi, \Omega''\chi'')$ vibronic states:

$$1s^{-1}\{\pi_t^*/\sigma_t^*/\pi_c^*\}\left(^1\Pi/\ ^1\Sigma^+/\ ^1\Pi, \Omega_r\chi_r\right) \rightarrow \begin{cases} 1s_t^2 1s_c^2 7\sigma^1 2\pi^4 \left(A\ ^2\Sigma^+, \Omega'\chi'\right) + \varepsilon\ell m\mu, \\ 1s_t^2 1s_c^2 7\sigma^2 2\pi^3 \left(X\ ^2\Pi, \Omega''\chi''\right) + \varepsilon\ell m\mu. \end{cases} \quad (2)$$

Here $\varepsilon\ell m\mu$ are the quantum numbers of the photoelectron partial waves in the asymptotical region [33,34] with the kinetic energy ε and fixed projections m and μ of the orbital angular momentum ℓ and spin s, respectively, on a chosen quantization axis.

Alternatively, the same final ionic states can be populated from the N_2O ground state via the weak direct photoionization channel:

$$1s_t^2 1s_c^2 7\sigma^2 2\pi^4 \left(X\ ^1\Sigma^+, \Omega_0\chi_0\right) + \hbar\omega \rightarrow \begin{cases} 1s_t^2 1s_c^2 7\sigma^1 2\pi^4 \left(A\ ^2\Sigma^+, \Omega'\chi'\right) + \varepsilon\ell m\mu, \\ 1s_t^2 1s_c^2 7\sigma^2 2\pi^3 \left(X\ ^2\Pi, \Omega''\chi''\right) + \varepsilon\ell m\mu. \end{cases} \quad (3)$$

Obviously, the resonant channel (1) and (2) and the direct channel (3) superimpose and interfere. Finally, the $A\ ^2\Sigma^+, \Omega'\chi'$ states of the N_2O^+ ion decay further via emission of a fluorescence photon of energy hc/λ into the $X\ ^2\Pi, \Omega''\chi''$ states:

$$1s_t^2 1s_c^2 7\sigma^1 2\pi^4 \left(A\ ^2\Sigma^+, \Omega'\chi'\right) \rightarrow 1s_t^2 1s_c^2 7\sigma^2 2\pi^3 \left(X\ ^2\Pi, \Omega''\chi''\right) + hc/\lambda. \quad (4)$$

III. EXPERIMENT

The present experiments were performed in two parts. The electron spectra were measured at the BW3 beamline of DORIS III at DESY, Helmholtz-Zentrum Hamburg. The beamline was equipped with a SX 700 monochromator using 1200 lines/mm gold-coated grating, in order to achieve a bandwidth of the exciting photons of about 125 meV full width at half maximum (FWHM) at 400 eV. The monochromatized synchrotron radiation intersected an effusive jet of N_2O molecules at room temperature and at a pressure of about 0.1 μbar. The exciting-photon energy was varied in steps of 0.1 eV and calibrated to the known energy positions of the core-excited states of N_2O [9,17].

The electrons were detected by an angle-resolving photoelectron spectrometer (ARPES), which is built of 16 individually working electron time-of-flight spectrometers mounted in a gold-coated aluminum ring. Each spectrometer possesses an angular acceptance of 0.2% of 4π, summing up to 3.6% solid angle for the whole setup. The gold coating of the mounting minimizes charge effects and can be used to apply a potential, needed for high-voltage retardings of the spectrometers. In essence, each spectrometer consists of four insulated, mounted drift paths, a bias mesh, a z stack of microchannel plates (MCPs) and an anode. From the interaction region to the first MCP the length totals to $\approx$140 mm. To enhance the electron-energy resolution of the spectrometers at a given time resolution, an overall retarding potential of 380 V was applied. The different parts of the drift tube were additionally optimized for energy resolution and transmission efficiency. In order to significantly reduce noise, the bias mesh was used to repel zero-energy electrons. The electron angular distribution parameters were obtained by fitting the intensities measured by 16 detectors with a Legendre polynomial expansion. The spectrometer was calibrated by measuring angular distribution of the Ne $2p$ photoelectron line [35]. A more detailed description of this experimental setup, calibration, and data processing can be found in [36].

The fluorescence spectra were measured at the variable polarization planar elliptical undulator UE56/2-PGM-1 beamline at Helmholtz-Zentrum Berlin. A 400 lines/mm grating and a slit width of 100 μm were used to monochromatize the synchrotron radiation resulting in a bandwidth of about 125 meV FWHM at 404 eV. It is then focused by the last beamline refocusing mirror via a differential pumping station into the interaction cell filled with N_2O gas at room temperature and at a pressure of 50 μbar. The photocurrent on the mirror is used to measure the incident photon flux. Insulated, mounted apertures confine the target cell. The total ion yield is measured at one aperture by applying a voltage to the other. An integrated photodiode collects the transmitted radiation.

Photon-induced fluorescence spectroscopy (PIFS) [37] experiments were carried out as described in detail for angle-unresolved [38–40] and angle resolved [28,31] studies of molecules. The fluorescence angular distribution parameters have been determined by the setup geometry and procedure described in [28]. In particular, the fluorescence light escapes the target cell through the two exit slits, one parallel and the other perpendicular to the electric field vector of the exciting linearly polarized radiation. It is then dispersed by a commercial type 225 McPherson 1-m-normal-incident monochromator equipped with 600 lines/mm grating and recorded by position-sensitive single-photon-counting MCP detectors. A commercial Quantar borosilicate encapsulated

multialkali-metal (S20: Na-K-Sb-Cs) z-stack detector was used. The fluorescence wavelengths were calibrated using well-known fluorescence lines of noble gases. With this setup, a wavelength resolution of up to $\Delta\lambda = 0.06$ nm can be achieved [41].

The polarization of the fluorescence radiation in the visible spectral range (350–700 nm) was analyzed by a Wollaston prism in front of the detector [42]. It splits up the linearly polarized fluorescence into two components, one polarized parallel $I_\parallel$ and one perpendicular $I_\perp$ to the electric field vector of the exciting synchrotron radiation. Because of the angular separation of about 5°, which is symmetric with respect to the optical axis, the two components leaving the Wollaston prism can be focused on the same detector with a displacement and, thus, recorded simultaneously. For the fluorescence observed perpendicular to the exciting-photon beam and perpendicular to the electric field vector of the linearly polarized exciting radiation, its polarization P is connected with the respective angular distribution parameter $\beta 2$ as [43]

$$P = \frac{I_\parallel - I_\perp}{I_\parallel + I_\perp} = \frac{3\beta 2}{\beta 2 - 2}. \tag{5}$$

Straightforwardly, the total fluorescence intensity I and the fluorescence anisotropy parameter $\beta 2$ can be obtained via [43]

$$I = \frac{2}{3}(2I_\perp + I_\parallel) \text{ and } \beta 2 = \frac{I_\perp - I_\parallel}{2I_\perp + I_\parallel}. \tag{6}$$

IV. THEORY

The differential cross section for photoelectrons emitted from randomly oriented molecules ionized by linearly polarized light is given by [33,34,44]

$$\frac{d\sigma_{\Omega_1\chi_1}(\omega)}{d\Omega} = \frac{\sigma_{\Omega_1\chi_1}(\omega)}{4\pi}\left[1 + \beta^e_{\Omega_1\chi_1}(\omega)P_2(\cos\theta)\right]. \tag{7}$$

Here θ is the angle between the electric field vector of the linearly polarized radiation and the direction of propagation of the outgoing electron emitted into the solid angle $d\Omega$. In order to derive equations for the total photoionization cross section $\sigma_{\Omega_1\chi_1}$ and the electron angular distribution parameter $\beta^e_{\Omega_1\chi_1}$ for arbitrary polyatomic molecules, we used the theoretical approach outlined in our previous works for diatomic molecules [28,45]. The presently obtained results are consistent with the previously published ones [34,44] and explicitly read

$$\sigma_{\Omega_1\chi_1}(\omega) = \sum_{\Omega_0\Omega_1}\sum_{\ell m}\sum_{\mu k}|D_k(\Omega_0,\Omega_1\chi_1\varepsilon\ell m\mu)|^2, \tag{8}$$

$$\begin{aligned}\beta^e_{\Omega_1\chi_1}(\omega) = {} & \frac{1}{\sigma_{\Omega_1\chi_1}(\omega)}\sum_{\Omega_0\Omega_1}\sum_{\ell m}\sum_{\ell' m'}\sum_{kk'}\sum_{\mu}(i)^{\ell+\ell'} \\ & \times\sqrt{30(2\ell+1)(2\ell'+1)}(-1)^{\ell'+m+k}e^{i(\delta_{\ell m}-\delta_{\ell' m'})} \\ & \times\begin{pmatrix}\ell & \ell' & 2\\ 0 & 0 & 0\end{pmatrix}\begin{pmatrix}\ell & \ell' & 2\\ -m & m' & k-k'\end{pmatrix} \\ & \times\begin{pmatrix}1 & 1 & 2\\ k & -k' & k'-k\end{pmatrix}D_k(\Omega_0,\Omega_1\chi_1\varepsilon\ell m\mu) \\ & \times D^*_{k'}(\Omega_0,\Omega_1\chi_1\varepsilon\ell' m'\mu),\end{aligned} \tag{9}$$

where $\delta_{\ell m}$ is the phase shift of the electron partial wave.

The total photoionization amplitude is given by the coherent sum of the direct amplitude for the transition (3) and the resonant amplitudes for all possible transitions (1) and (2) as [28–31]

$$\begin{aligned}& D_k(\Omega_0,\Omega_1\chi_1\varepsilon\ell m\mu) \\ & = \sqrt{\frac{4\pi^2\alpha a_0^2\omega^{\pm1}}{3g_{\Omega_0}}}\Bigg\{\langle\Omega_1\chi_1\varepsilon\ell m\mu|\mathbf{d}_k|\Omega_0\chi_0\rangle \\ & \quad + \sum_{\Omega_r\chi_r}\frac{\langle\Omega_1\chi_1\varepsilon\ell m\mu|\mathbf{H^{ee}}|\Omega_r\chi_r\rangle\langle\Omega_r\chi_r|\mathbf{d}_k|\Omega_0\chi_0\rangle}{\omega - E_{\Omega_r\chi_r} + i\Gamma_{\Omega_r\chi_r}/2}\Bigg\}.\end{aligned} \tag{10}$$

Here $\alpha = 1/137.036$ is the fine structure constant, $\omega^{\pm1}$ represents, respectively, the length or velocity forms of the dipole transition operator; g_{Ω_0} is the statistical weight of the initial electronic state; the square of the Bohr radius $a_0^2 = 28.0028$ Mb converts atomic units for cross sections into Mb; and $E_{\Omega_r\chi_r}$ and $\Gamma_{\Omega_r\chi_r}$ are the energy positions and Auger decay widths of the intermediate states, respectively. The LVI is accounted for in Eq. (10) via the summation over index χ_r, whereas the sum of the first and second terms in the braces together with the summation over index Ω_r in the second term incorporate the ESI.

Applying the theoretical approach [28,45], we have derived equations for the differential fluorescence intensities emitted in step (4) by randomly oriented arbitrary polyatomic molecules excited by linearly polarized light,

$$\frac{dI^{\Omega_2\chi_2}_{\Omega_1\chi_1}(\omega)}{d\Omega} = \frac{I^{\Omega_2\chi_2}_{\Omega_1\chi_1}(\omega)}{4\pi}\left[1 + \beta 2^{\Omega_2\chi_2}_{\Omega_1\chi_1}(\omega)P_2(\cos\theta)\right]. \tag{11}$$

Here the angle θ defines the direction of detection of the fluorescence radiation with respect to the polarization vector of the exciting radiation. The total intensity $I^{\Omega_2\chi_2}_{\Omega_1\chi_1}$ can be computed as the product of the total cross section (8) and the fluorescence yield $\chi^{\Omega_2\chi_2}_{\Omega_1\chi_1}$ [28],

$$I^{\Omega_2\chi_2}_{\Omega_1\chi_1}(\omega) = \sigma_{\Omega_1\chi_1}(\omega)\,\chi^{\Omega_2\chi_2}_{\Omega_1\chi_1}, \tag{12}$$

and the fluorescence angular distribution parameter $\beta 2^{\Omega_2\chi_2}_{\Omega_1\chi_1}$ is given by

$$\begin{aligned}\beta 2^{\Omega_2\chi_2}_{\Omega_1\chi_1}(\omega) = {} & \left[\sigma_{\Omega_1\chi_1}(\omega)\sum_{\Omega_2 q}|\langle\Omega_2\chi_2|\mathbf{d}_q|\Omega_1\chi_1\rangle|^2\right]^{-1} \\ & \times\sum_{\Omega_0\Omega_2}\sum_{qq'}\sum_{\Omega_1\Omega_1'}\sum_{\ell m\mu}\sum_{kk'}3(-1)^{k+q'+1} \\ & \times\begin{pmatrix}1 & 1 & 2\\ k & -k' & q-q'\end{pmatrix}\begin{pmatrix}1 & 1 & 2\\ q & -q' & k-k'\end{pmatrix} \\ & \times\langle\Omega_2\chi_2|\mathbf{d}_{q'}|\Omega_1'\chi_1\rangle^*D^*_{k'}(\Omega_0,\Omega_1'\chi_1\varepsilon\ell m\mu) \\ & \times\langle\Omega_2\chi_2|\mathbf{d}_q|\Omega_1\chi_1\rangle D_k(\Omega_0,\Omega_1\chi_1\varepsilon\ell m\mu).\end{aligned} \tag{13}$$

We note that Eqs. (9) and (13) derived for polyatomic molecules are very similar to the corresponding equations obtained for diatomic molecules [28,45] with the following main difference. Whereas quantum numbers m and μ stand here for the projections of the orbital angular momentum ℓ and spin s of a photoelectron on the chosen quantization axis (e.g., the highest-order rotational axis of the point group to which the molecule belongs), the symbol Ω_i is not a quantum number of

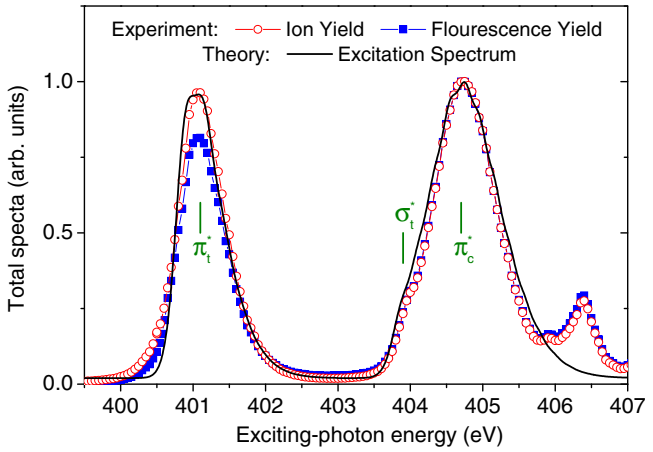

FIG. 1. (Color online) The total ion and fluorescence yields measured in the present work in the vicinity of the π_t^*, σ_t^*, and π_c^* resonances of N_2O (the energy positions are indicated by vertical bars) together with the presently computed broadband excitation spectrum obtained via the three-dimensional nuclear dynamics calculations. All spectra are normalized at the maximum. For further details, see Secs. III and IV.

the electronic states of an arbitrary polyatomic molecule and it is just used here to numerate different electronic states. As a consequence, no particular selection rules can be applied for the transition amplitude (10), like it was possible in diatomics, where, e.g., $\sigma \to \sigma$ transitions correspond to $k,q = 0$ and $\sigma \to \pi$ to $k,q = \pm 1$. Therefore, all summations in Eqs. (9) and (13) over indices $\{\Omega,m,\mu,k,q\}$ must be performed fully and independently.

In its ground electronic state the N_2O molecule is linear [46]. Equilibrium geometries of the presently considered ground X and first excited A electronic states of the N_2O^+ ion are also linear [46]. However, the core-excited states have stable bent structures with large N-N-O bending angles [17] of around 136° for π_t^* and 114° for π_c^*. Therefore, in order to accurately compute the excitation spectrum (see Fig. 1), it was important to include the bending dynamical mode in the nuclear dynamic simulations. Calculations of the three-dimensional nuclear dynamics accompanying the cascade decay (1)–(4) in the N_2O molecule were carried out by the multiconfiguration time-dependent Hartree (MCTDH) method [47] and code [48]. The potential energy surfaces involved in the nuclear dynamics were obtained by the full valence complete active space multiconfiguration self-consistent field calculations with subsequent multireference configuration interaction approach, as described in detail in [49,50]. As in our previous studies of the core-excited molecules [28,39,40], the equivalent core "$Z + 1$" approximation was used for the intermediate resonances.

The electronic part of calculations, which involves accurate wave functions of the molecular core orbitals, excited electronic states, and the partial photoelectron continuous waves, was carried out by the single-center (SC) method and code [51,52]. Briefly, one-particle molecular orbitals are represented in the SC method via expansions over spherical harmonics with respect to a single molecular center. Molecular orbitals of the photoelectron in the continuum are obtained by numerical solution of a system of coupled Hartree-Fock equations with accurate molecular field potentials provided by the representation of the occupied molecular orbitals as the linear combination of atomic orbitals (MO LCAO). The obtained numerical solutions are renormalized in order to satisfy the condition of observable incoming photoelectron partial waves. In the calculations of the electronic transition matrix elements, the monopole relaxation of the molecular orbital was accounted for similar to our previous studies of core-excited molecules [28–31]. The calculations were performed at the equilibrium internuclear geometry of the ground electronic state of N_2O.

A typical time scale for the nuclear bending motion in N_2O can be estimated from the corresponding energy constant for the ground electronic state ($\omega_{\text{bend}} \approx 589$ cm^{-1} [46]) as $\tau_{\text{bend}} = 2\pi/\omega_{\text{bend}} \approx 57$ fs. This period is about 10 times longer than the natural lifetime of the core-excited resonances $\tau_{\text{dec}} = 1/\Gamma_A \approx 5.3$ fs, provided that the Auger decay width of the core-excited N_2O is similar to that of NO ($\Gamma_A = 125$ meV [53]). Therefore, the N_2O molecule has practically no time to bend in the core-excited state during its Auger decay, and the final ionic states are populated at nearly linear geometry. According to the calculations, at 15 fs after its excitation (when the Auger decay is essentially completed), the nuclear wave packet in the core-excited states has its maximum around the bending angle of 165°.

As a consequence, the Renner-Teller effect of a vibronic coupling via the bending dynamical mode has relatively weak impact on the resonant Auger electron spectra of N_2O: It results in a slight redistribution of the vibrational intensity [8,54], which becomes visible in the vibrationally resolved detection regime. It is, however, more relevant for the angle resolved ion-yield fragmentation spectra of the core-excited states of N_2O [17,18], a process which explicitly involves nuclear dissociation mechanism of the highly excited final ionic states with essentially bent geometry. In the present calculations of the angle resolved decay spectra, it is important to treat electronic states of π symmetry as two nondegenerate states, i.e., as in-plane $\pi(a')$ and out-of-plane $\pi(a'')$ orbitals split by the Renner-Teller effect, since summations in Eqs. (9) and (13) must be performed only over degenerate electronic states Ω_0, Ω_1, and Ω_2.

V. RESULTS AND DISCUSSION

The recorded total ion yield as a function of the exciting-photon energy and the fluorescence excitation function for undispersed fluorescence between 350 and 700 nm are shown in Fig. 1 by open circles and solid squares, respectively. In the exciting-photon energy range of 399.5–407 eV, the π_t^*, σ_t^*, and π_c^* resonances are the dominant excitations of N_2O. Their energy positions are marked in the figure by vertical lines. At the energies above 406 eV, clear fingerprints of Rydberg excitations [6,17] are seen in the experimental spectra. These states were, however, excluded from the present theoretical consideration. The theoretical broadband excitation spectrum obtained in the present work by a full three-dimensional nuclear dynamics calculations (including two vibrational and one bending modes) is also shown in Fig. 1 by the solid line for comparison.

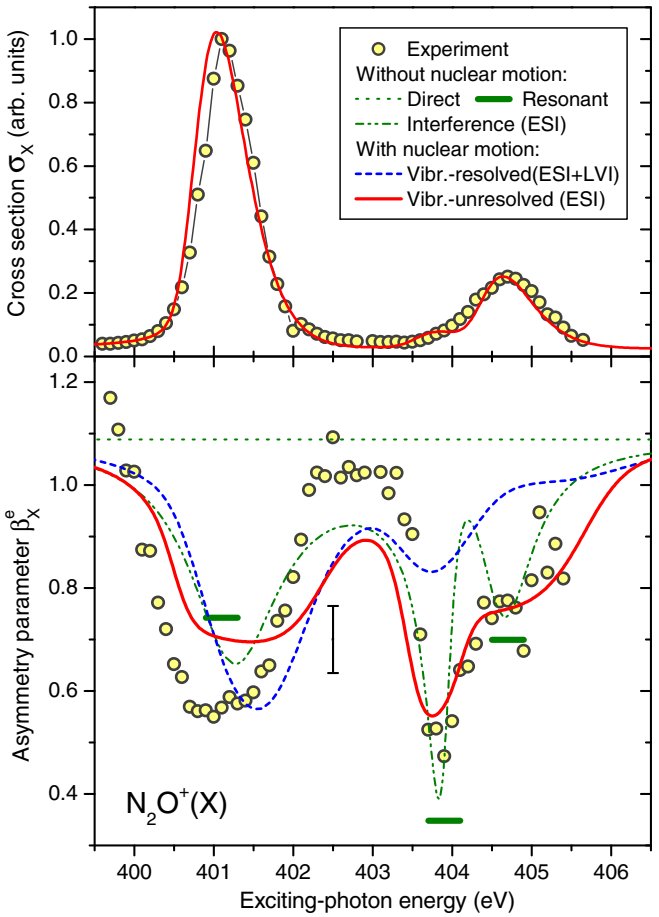

FIG. 2. (Color online) Relative cross section for the population of the $N_2O^+(X)$ final ionic state (top panel) and photoelectron angular distribution parameter (bottom panel) measured in the present work in the vibrationally unresolved regime and computed in different approximations (see legends and text for details). Experimental and theoretical cross sections are equalized at their maxima, whereas no normalization for asymmetry parameter is required. The typical experimental error (1σ) is shown in the bottom panel by the vertical bar.

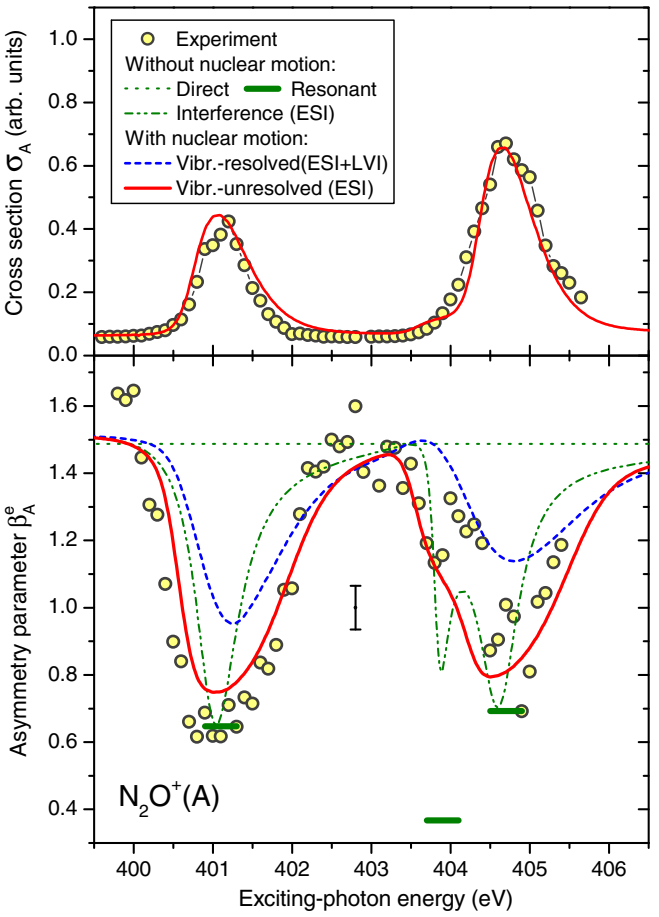

FIG. 3. (Color online) Parameters measured and computed for the $N_2O^+(A)$ final ionic state (see notations in Fig. 2).

We first discuss the resonant Auger electron spectra of N_2O, which are shown in Figs. 2 and 3 for the $N_2O^+(X)$ and $N_2O^+(A)$ final ionic states, respectively. The corresponding total (angular averaged) cross sections and angular distribution parameters are depicted in the top and bottom panels of these figures, respectively. The experimental data are shown by circles. One should note that the present electron spectra were recorded in the vibrationally unresolved mode, since individual vibrational levels of the final ionic states strongly overlap and can hardly be resolved [9]. In order to interpret the present angle resolved experiment, we performed calculations of the cross sections and angular distribution parameters in different approximations.

In the first step we neglected the nuclear motion and included only electronic transitions. The angular distribution parameters $\beta^e_{\Omega_1}(\omega)$ computed individually for each of the π_t^*, σ_t^*, and π_c^* resonances (*Resonant* approximation) and only for the direct transition (*Direct* approximation) are shown in the bottom panels of Figs. 2 and 3 by thick horizontal bars at the corresponding energy positions and by dotted horizontal lines, respectively. Note, these individual $\beta^e_{\Omega_1}(\omega)$ are independent of the exciting-photon energy [28–31]. The interference between direct and all resonant electronic channels (i.e., ESI) induces sharp exciting-photon energy dependencies (dispersions) of the computed $\beta^e_{\Omega_1}(\omega)$ parameters across the positions of the electronic resonances [*Interference(ESI)* approximation, dash-dot-dotted curve].

The typical impact of the nuclear dynamics and of the underlying LVI effects on the computed angle resolved electron spectra is demonstrated in the lower panels of Figs. 2 and 3 by the dashed curves [*Vibr.-resolved(ESI+LVI)* approximation]. For both ionic states $N_2O^+(X)$ and $N_2O^+(A)$, the computed angular distribution parameters $\beta^e_{\Omega_1}(\omega)$ are shown only for the ground vibronic states $X,\chi'(000)$ and $A,\chi''(000)$, which are the most intense vibronic lines in the corresponding resonant Auger electron spectra [9]. One can see from these figures that the sharp dispersions of the $\beta^e_{\Omega_1}(\omega)$ parameters emerging due to ESI become now essentially broader and the corresponding interference structures in $\beta^e_{\Omega_1}(\omega)$ are somewhat washed out (cf., dash-dot-dotted and dashed curves).

In order to reproduce the angle resolved resonant Auger electron spectra recorded in the present experiment in the vibrationally unresolved mode, one has to perform summations of the computed partial cross sections (8) and angular

distribution parameters (9) over the vibrational quantum number of the final ionic state χ_1 at each photon energy ω as follows:

$$\sigma_{\Omega_1} = \sum_{\chi_1} \sigma_{\Omega_1\chi_1}, \tag{14}$$

$$\beta^e_{\Omega_1} = \frac{1}{\sigma_{\Omega_1}} \sum_{\chi_1} \beta^e_{\Omega_1\chi_1}\, \sigma_{\Omega_1\chi_1}. \tag{15}$$

In practice, it requires calculations of the partial data for all final vibronic states $\Omega_1\chi_1$, which is a cumbersome issue. One can, however, perform this summations analytically even in the presence of ESI and simplify, thereby, calculations significantly. This analytical procedure is outlined in the Appendix.

By inspecting the final Eqs. (A9) and (A10), one can see that the averaging destroys possible LVI effects (note that summations over index χ_r are carried out there incoherently). Therefore, LVI cannot be observed in the vibrationally unresolved spectra even for strongly overlapping intermediate vibronic states χ_r. The corresponding total cross sections and angular distribution parameters averaged over vibrational levels of the final ionic states are shown in Figs. 2 and 3 by solid curves [*Vibr.-unresolved (ESI)* approximation]. A very good qualitative (and even overall quantitative) agreement between the averaged theoretical and the vibrationally unresolved experimental data can be seen from these figures; e.g., the computed dispersions of $\beta^e_{\Omega_1}(\omega)$ parameters become significantly broader and they are very similar to the experimental dispersions around the two overlapping σ_t^* and π_c^* electronic resonances.

We now turn to the angle resolved fluorescence spectra of N_2O^+. In the present experiment, the two most intense fluorescence bands $A,\chi'(000) \rightarrow X,\chi''(000)$ and $A,\chi'(000) \rightarrow X,\chi''(100)$ [55,56] have been clearly resolved and analyzed. The significantly weaker fluorescence bands (001) → (101), (100) → (200), and (010) → (010) were also resolved, but, owing to a very low signal-to-noise ratio, they are not discussed below. It is known [28–31] that angular distribution parameters for fluorescence $\beta 2^{\Omega''\chi''}_{\Omega'\chi'}(\omega)$ are independent of the vibrational level χ'' of the final fluorescence state Ω'' and are, therefore, equal for the two presently resolved bands with the same initial fluorescence state $A,\chi'(000)$. The presently measured angular distribution parameter $\beta 2^X_A$ for the two fluorescence bands $A,\chi'(000) \rightarrow X,\chi''$ is shown in Fig. 4 by circles. Because of the significantly smaller count rates, the fluorescence measurements are usually much more time consuming than detecting of electrons. Therefore, not the whole exciting-photon energy range of interest was covered in the experiment. At first, angle resolved fluorescence spectra were recorded and analyzed at three exciting-photon energies around the positions of the resonances where the fluorescence signal is expected to be significant. On the basis of a preliminary analysis of the acquired data, we have decided to pay a particular attention to the energy range around the two overlapping σ_t^* and π_c^* electronic resonances, where larger values of the measured $\beta 2^X_A$ parameter and substantial interference effects were expected.

The $\beta 2^{X\chi''}_{A(000)}(\omega)$ parameter computed in the present work without accounting for the nuclear dynamics is depicted in Fig. 4 by dash-dot-dotted curve [*Interference(ESI)* approximation]. As one can see, it exhibits very sharp dispersions across the positions of the electronic resonances. It also approaches individual contribution from the direct ionization channel in the energy detuning regime (dotted curve, *Direct* approximation) and follows individual contributions of the electronic resonances in the on-resonance excitation regime (thick horizontal bars, *Resonant* approximation).

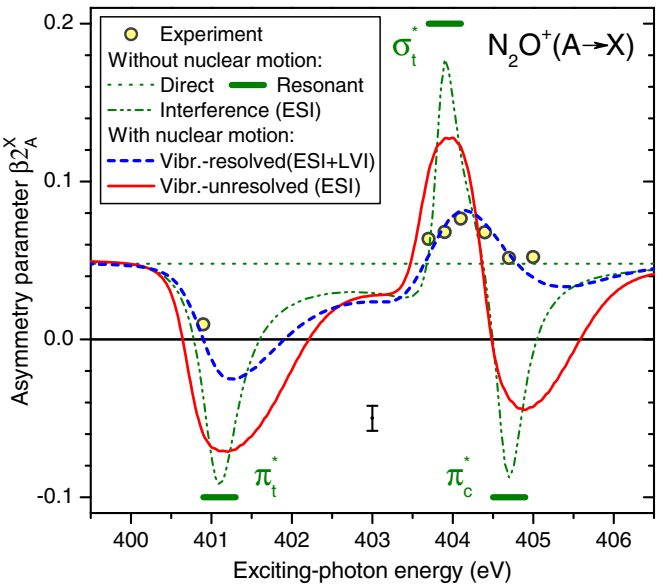

FIG. 4. (Color online) Angular distribution parameter for the $A,\chi'(000) \rightarrow X,\chi''$ fluorescence bands progression of the N_2O^+ ion measured in the present work in the vibrationally resolved regime and computed in different approximations (see legend and also text for details). The typical experimental error (1σ) is shown by the vertical bar.

The $\beta 2^{X\chi''}_{A(000)}(\omega)$ parameter computed with accounting for the nuclear motion and, thus, with LVI is depicted in Fig. 4 by dashed curve [*Vibr.-resolved(ESI+LVI)* approximation]. As is evident from this figure, the computed dispersions across the resonances become significantly broadened (cf., dash-dot-dotted and dashed curves). Importantly, the computed $\beta 2^{X\chi''}_{A(000)}(\omega)$ parameter agrees very well with the measured one (cf., dashed curve and circles): The corresponding energy dependencies across the two overlapping σ_t^* and π_c^* electronic resonances and a single-energy-point values around the π_t^* resonance are in a very good qualitative and even quantitative agreement. A slight disagreement between the computed and measured $\beta 2^{X\chi''}_{A(000)}$ values at $\omega = 405$ eV (last experimental point in Fig. 4) can be attributed to the influence of the higher-lying Rydberg excitations [6,17], which were not included in the present calculations.

For completeness, the theoretical $\beta 2^X_A(\omega)$ parameter averaged over all fluorescence bands is also shown in Fig. 4 by the solid curve [*Vibr.-unresolved(ESI)* approximation]. As was discussed above, this averaging corresponds to the vibrationally unresolved experiment and it eliminates possible underlying LVI effects. A large quantitative disagreement between the averaged theoretical and experimental parameters

(cf., solid curve and circles) illustrates the important role of LVI in the formation of the vibrationally and angularly resolved fluorescence spectra.

VI. CONCLUSIONS

Angle resolved electron-fluorescence cascade decay spectra of the core-excited terminal and central nitrogen atoms of N_2O are studied experimentally and theoretically. In the experiment, relative cross sections and angular distribution parameters for the production of the $N_2O^+(X)$ and $N_2O^+(A)$ ions were measured in the vicinity of the $N_t(1s \to \pi^*)$, $N_t(1s \to \sigma^*)$, and $N_c(1s \to \pi^*)$ resonances in the vibrationally unresolved mode by ARPES. Simultaneously, angular distributions of the vibrationally resolved intense fluorescence lines of the $N_2O^+(A \to X)$ radiative decay subsequent to the resonant Auger process were measured by PIFS.

In the theory, general equations for the angle resolved photoelectron and fluorescence spectra in polyatomic molecules are reported. The corresponding electronic transition matrix elements were computed by the SC method, whereas nuclear dynamics accompanying the cascade decay in N_2O by the MCTDH method. In the calculations, LVI and ESI of the weak direct and different resonant electronic transitions were taken into account. How to analytically average cross sections and angular distribution parameters over the final vibronic states in the general case of ESI is also shown. Such averaging corresponds to observation in the vibrationally unresolved regime and it destroys LVI in the angle resolved electron spectra.

The present experimental and theoretical angle resolved electron-fluorescence cascade spectra agree very well. The ESI induces long-energy-range dispersions of the computed photoelectron and fluorescence angular distribution parameters, which are evident in the experiment. Averaging of the computed angular distribution parameters of photoelectrons over the final vibronic states makes these dispersions even broader and brings the theoretical parameters in a good agreement with the experimental ones. Finally, strong LVI effects can be clearly identified in the vibrationally resolved angular distribution parameters of fluorescence, and they bring the computed asymmetry parameters in a very good quantitative agreement with the measured ones. These two important effects were identified in the present work due to the possibility to simultaneously analyze the angle resolved electron and fluorescence spectra.

ACKNOWLEDGMENTS

This work was supported by the State Hessen Initiative for the Development of Scientific and Economic Excellence (LOEWE) within the focus project Electron Dynamic of Chiral Systems (ELCH). Financial support by the Deutsche Forschungsgemeinschaft (DFG Project No. DE 2366/1-1) is gratefully acknowledged. M.I. acknowledges financial support by the Volkswagen foundation within the Peter Paul Ewald fellowship. We thank Helmholtz-Zentrum Berlin (HZB) and Helmholtz-Zentrum Hamburg (HZH) for the allocation of synchrotron radiation beamtime. We also thankfully acknowledge the financial support from HZB and HZH.

APPENDIX: VIBRATIONALLY UNRESOLVED RESONANT AUGER DECAY SPECTRUM

In this Appendix we perform an analytical summation of the angle resolved resonant Auger electron spectra, Eqs. (14) and (15), over the vibrational quantum numbers of the final ionic state, which corresponds to the vibrationally unresolved measurements. For transparency, we restrict our consideration to the direct and only one resonant electronic channel, imply the Franck-Condon approximation, and introduce simplified notations for the transition amplitude (10),

$$D_{j\chi_1} = d_j \langle \chi_1 | \chi_0 \rangle + \sum_{\chi_r} \frac{V_j D \langle \chi_1 | \chi_r \rangle \langle \chi_r | \chi_0 \rangle}{\omega - E_{\chi_r} + i\Gamma_{\chi_r}/2}, \tag{A1}$$

where index j numerates photoionization channels, and d_j, D, and V_j stand for the electronic amplitudes for the direct ionization, excitation, and subsequent Auger decay of the resonance, respectively. With the help of these notations and definitions (8) and (9), Eqs. (14) and (15) can be rewritten as (index Ω_1 is omitted here and below for brevity)

$$\sigma = \sum_{\chi_1} \sigma_{\chi_1} \quad \text{with} \quad \sigma_{\chi_1} = \sum_j |D_{j\chi_1}|^2, \tag{A2}$$

$$\beta^e = \frac{1}{\sigma} \sum_{\chi_1} \beta^e_{\chi_1} \sigma_{\chi_1} \quad \text{with} \quad \beta^e_{\chi_1} \sigma_{\chi_1} = \sum_{ij} \alpha_{ij} D^*_{i\chi_1} D_{j\chi_1}, \tag{A3}$$

where α_{ij} is the complex coefficient in Eq. (9). Below, we explicitly perform analytical summation over χ_1 only for the angular distribution parameter (A3), and for the total cross section (A2) only the final result will be listed.

Inserting Eq. (A1) in Eqs. (A3) we obtain

$$\beta^e = \frac{1}{\sigma} \sum_{\chi_1} \sum_{ij} \alpha_{ij} D^*_{i\chi_1} D_{j\chi_1} = \frac{1}{\sigma} \sum_{ij} \alpha_{ij} \left\{ \sum_{\chi_1} d_i^* d_j \langle \chi_0 | \chi_1 \rangle \langle \chi_1 | \chi_0 \rangle + \sum_{\chi_1} \sum_{\chi_r} d_i^* V_j D \frac{\langle \chi_0 | \chi_1 \rangle \langle \chi_1 | \chi_r \rangle \langle \chi_r | \chi_0 \rangle}{\omega - E_{\chi_r} + i\Gamma_{\chi_r}/2} \right.$$

$$\left. + \sum_{\chi_1} \sum_{\chi_r} V_i^* D^* d_j \frac{\langle \chi_0 | \chi_r \rangle \langle \chi_r | \chi_1 \rangle \langle \chi_1 | \chi_0 \rangle}{(\omega - E_{\chi_r} + i\Gamma_{\chi_r}/2)^*} + \sum_{\chi_1} \sum_{\chi_r \chi_r'} V_i^* D^* V_j D \frac{\langle \chi_0 | \chi_r' \rangle \langle \chi_r' | \chi_1 \rangle \langle \chi_1 | \chi_r \rangle \langle \chi_r | \chi_0 \rangle}{\left(\omega - E_{\chi_r'} + i\Gamma_{\chi_r'}/2\right)^* (\omega - E_{\chi_r} + i\Gamma_{\chi_r}/2)} \right\}. \tag{A4}$$

Implying the resolution of identity $I = \sum_{\chi_1} |\chi_1\rangle\langle\chi_1|$, orthogonality condition $\langle\chi_r'|\chi_r\rangle = \delta_{\chi_r'\chi_r}$, and multiplying the first term with unity $\sum_{\chi_r} |\langle\chi_r|\chi_0\rangle|^2 = 1$, we straightforwardly arrive at the following simple analytical result:

$$\beta^e = \frac{1}{\sigma}\sum_{ij}\alpha_{ij}\left\{d_i^* d_j \sum_{\chi_r}|\langle\chi_r|\chi_0\rangle|^2 + \sum_{\chi_r}\frac{d_i^* V_j D|\langle\chi_r|\chi_0\rangle|^2}{\omega - E_{\chi_r} + i\Gamma_{\chi_r}/2}\right.$$
$$\left. + \sum_{\chi_r}\frac{V_i^* D^* d_j|\langle\chi_r|\chi_0\rangle|^2}{(\omega - E_{\chi_r} + i\Gamma_{\chi_r}/2)^*} + \sum_{\chi_r}\frac{V_i^* D^* V_j D|\langle\chi_r|\chi_0\rangle|^2}{|(\omega - E_{\chi_r} + i\Gamma_{\chi_r}/2)|^2}\right\}. \quad \text{(A5)}$$

By introducing the new ionization amplitude

$$D_{j\chi_r} = \left(d_j + \frac{V_j D}{\omega - E_{\chi_r} + i\Gamma_{\chi_r}/2}\right)\langle\chi_r|\chi_0\rangle, \quad \text{(A6)}$$

Eq. (A5) takes on the following simple form:

$$\beta^e = \frac{1}{\sigma}\sum_{ij}\alpha_{ij}\sum_{\chi_r} D_{i\chi_r}^* D_{j\chi_r}. \quad \text{(A7)}$$

Proceeding in analogy, one can derive a similar result for the total cross section, which reads

$$\sigma = \sum_j\sum_{\chi_r}|D_{j\chi_r}|^2. \quad \text{(A8)}$$

As the final step, we introduce the partial ionization cross section σ_{χ_r} and the corresponding angular distribution parameter $\beta^e_{\chi_r}$ for an individual vibronic state χ_r of the intermediate resonance and straightforwardly arrive at the final working equations which replace the starting Eqs. (A2) and (A3):

$$\sigma = \sum_{\chi_r}\sigma_{\chi_r} \quad \text{with} \quad \sigma_{\chi_r} = \sum_j |D_{j\chi_r}|^2, \quad \text{(A9)}$$

$$\beta^e = \frac{1}{\sigma}\sum_{\chi_r}\beta^e_{\chi_r}\sigma_{\chi_r} \quad \text{with} \quad \beta^e_{\chi_r}\sigma_{\chi_r} = \sum_{ij}\alpha_{ij} D_{i\chi_r}^* D_{j\chi_r}. \quad \text{(A10)}$$

The main advantage of the final result (A9) and (A10) consists in the fact that the amplitude (A6) contains Franck-Condon factors only for the resonant excitation $\langle\chi_r|\chi_0\rangle$, whereas all those for the direct ionization $\langle\chi_1|\chi_0\rangle$ and Auger decay $\langle\chi_1|\chi_r\rangle$ were eliminated by performing summations over the complete set of the final vibronic states χ_1 and, thus, need not to be computed.

[1] M. Alagia *et al.*, Phys. Rev. A **71**, 012506 (2005).
[2] M. Ehara *et al.*, Chem. Phys. Lett. **438**, 14 (2007).
[3] F. P. Larkins, J. Chem. Phys. **86**, 3239 (1987).
[4] P. Bolognesi, M. Coreno, L. Avaldi, L. Storchi, and F. Tarantelli, J. Chem. Phys. **125**, 054306 (2006).
[5] G. R. Wright and C. E. Brion, J. Electron Spectrosc. Relat. Phenom. **3**, 191 (1974).
[6] K. C. Prince, L. Avaldi, M. Coreno, R. Camilloni, and M. de Simone, J. Phys. B **32**, 2551 (1999).
[7] F. P. Larkins, W. Eberhardt, I.-W. Lyo, R. Murphy, and E. W. Plummer, J. Chem. Phys. **88**, 2948 (1988).
[8] C. Miron *et al.*, J. Chem. Phys. **115**, 864 (2001).
[9] M. N. Piancastelli *et al.*, J. Phys. B **40**, 3357 (2007).
[10] T. LeBrun, M. Lavollée, M. Simon, and P. Morin, J. Chem. Phys. **98**, 2534 (1993).
[11] J. D. Bozek, N. Saito, and I. H. Suzuki, J. Chem. Phys. **98**, 4652 (1993).
[12] S.-Y. Chen, C.-I. Ma, D. M. Hanson, K. Lee, and D. Y. Kim, J. Electron Spectrosc. Relat. Phenom. **93**, 61 (1998).
[13] M. Machida, M. Lavollée, J. Randrianjafisoa, G. Laurent, M. Nagoshi, K. Okada, I. Koyano, and N. Saito, J. Chem. Phys. **120**, 3635 (2004).
[14] V. Schmidt, Rep. Prog. Phys. **55**, 1483 (1992).
[15] N. A. Cherepkov and S. K. Semenov, J. Phys. B **37**, 1267 (2004).
[16] M. Schmidbauer, A. L. D. Kilcoyne, K. J. Randall, J. Feldhaus, A. M. Bradshaw, M. Braunstein, and V. McKoy, J. Chem. Phys. **94**, 5299 (1991).
[17] J. Adachi, N. Kosugi, E. Shigemasa, and A. Yagishita, J. Chem. Phys. **102**, 7369 (1995).
[18] T. Tanaka *et al.*, Chem. Phys. Lett. **428**, 34 (2006).
[19] A. Cesar and H. Ågren, Phys. Rev. A **45**, 2833 (1992).
[20] F. K. Gel'mukhanov, L. N. Mazalov, and A. V. Kondratenko, Chem. Phys. Lett. **46**, 133 (1977).
[21] F. K. Gel'mukhanov and H. Ågren, Phys. Rep. **312**, 87 (1999).
[22] V. Carravetta, F. K. Gel'mukhanov, H. Ågren, S. Sundin, S. J. Osborne, A. Navas de Brito, O. Björneholm, A. Ausmees, and S. Svensson, Phys. Rev. A **56**, 4665 (1997).
[23] S. Sundin, F. K. Gel'mukhanov, H. Ågren, S. J. Osborne, A. Kikas, O. Björneholm, A. Ausmees, and S. Svensson, Phys. Rev. Lett. **79**, 1451 (1997).
[24] O. Björneholm, S. Sundin, S. Svensson, R. R. T. Marinho, A. Naves de Brito, F. K. Gel'mukhanov, and H. Ågren, Phys. Rev. Lett. **79**, 3150 (1997).
[25] R. Feifel, T. Tanaka, M. Hoshino, H. Tanaka, Y. Tamenori, V. Carravetta, and K. Ueda, Phys. Rev. A **74**, 062717 (2006).
[26] E. Kukk, J. D. Bozek, W. Cheng, R. F. Finka, A. A. Wills, and N. Berrah, J. Chem. Phys. **111**, 9642 (1999).
[27] H. Wang *et al.*, Chem. Phys. **289**, 31 (2003).
[28] Ph. V. Demekhin, I. D. Petrov, V. L. Sukhorukov, W. Kielich, P. Reiss, R. Hentges, I. Haar, H. Schmoranzer, and A. Ehresmann, Phys. Rev. A **80**, 063425 (2009); **81**, 069902 (2010).
[29] Ph. V. Demekhin, I. D. Petrov, T. Tanaka, M. Hoshino, H. Tanaka, K. Ueda, W. Kielich, and A. Ehresmann, J. Phys. B **43**, 065102 (2010).

[30] Ph. V. Demekhin, I. D. Petrov, V. L. Sukhorukov, W. Kielich, A. Knie, H. Schmoranzer, and A. Ehresmann, Phys. Rev. Lett. **104**, 243001 (2010).
[31] Ph. V. Demekhin, I. D. Petrov, V. L. Sukhorukov, W. Kielich, A. Knie, H. Schmoranzer, and A. Ehresmann, J. Phys. B **43**, 165103 (2010).
[32] A. Lindblad, V. Kimberg, J. Söderström, C. Nicolas, O. Travnikova, N. Kosugi, F. Gel'mukhanov, and C. Miron, New J. Phys. **14**, 113018 (2012).
[33] N. A. Cherepkov, J. Phys. B **14**, 2165 (1981).
[34] N. A. Cherepkov, Chem. Phys. Lett. **87**, 344 (1982).
[35] F. Wuilleumier and M. O. Krause, J. Electron Spectrosc. Relat. Phenom. **15**, 15 (1976).
[36] M. Ilchen, Ph.D. thesis, TU Berlin, 2012, http://opus.kobv.de/tuberlin/volltexte/2012/3586/
[37] H. Schmoranzer, H. Liebel, F. Vollweiler, R. Müller-Albrecht, A. Ehresmann, K.-H. Schartner, and B. Zimmermann, Nucl. Instrum. Methods Phys. Res. A **467–468**, 1526 (2001).
[38] H. Liebel, A. Ehresmann, H. Schmoranzer, Ph. V. Demekhin, B. M. Lagutin, and V. L. Sukhorukov, J. Phys. B **35**, 895 (2002).
[39] A. Ehresmann *et al.*, J. Phys. B **39**, 283 (2006).
[40] A. Ehresmann, W. Kielich, L. Werner, Ph. V. Demekhin, D. V. Omel'yanenko, V. L. Sukhorukov, K.-H. Schartner, and H. Schmoranzer, Eur. Phys. J. D **45**, 235 (2007).
[41] A. Knie, N. Burbank, P. Schmidt, C. Ozga, and A. Ehresmann, J. Electron Spectrosc. Relat. Phenom. **185**, 492 (2012).
[42] B. Zimmermann *et al.*, J. Phys. B **33**, 2467 (2000).
[43] E. G. Berezhko and N. M. Kabachnik, J. Phys. B **10**, 2467 (1977).
[44] B. Ritchie, Phys. Rev. A **13**, 1411 (1976).
[45] Ph. V. Demekhin, I. D. Petrov, and A. Ehresmann, Pys. Rev. A **82**, 041401(R) (2010).
[46] G. Herzberg, *Molecular Spectra and Molecular Structure. III. Electronic Spectra and Electronic Structure of Polyatomic Molecules* (Van Nostrand Reinhold, New York, 1966).
[47] H.-D. Meyer, U. Manthe, and L. S. Cederbaum, Chem. Phys. Lett. **165**, 73 (1990).
[48] G. A. Worth, M. H. Beck, A. Jäckle, and H.-D. Meyer, The Multiconfiguration Time-dependent Hartree (MCTDH) Package; see http://www.pci.uni-heidelberg.de/cms/mctdh.html
[49] A. Ehresmann, H. Liebel, H. Schmoranzer, B. Zimmermann, S. Kammer, K.-H. Schartner, Ph. V. Demekhin, and V. L. Sukhorukov, J. Phys. B **36**, 3669 (2003).
[50] A. Ehresmann *et al.*, J. Phys. B **37**, 4405 (2004).
[51] Ph. V. Demekhin, D. V. Omel'yanenko, B. M. Lagutin, V. L. Sukhorukov, L. Werner, A. Ehresmann, K.-H. Schartner, and H. Schmoranzer, Opt. Spectrosc. **102**, 318 (2007).
[52] Ph. V. Demekhin, V. L. Sukhorukov, and A. Ehresmann, J. Chem. Phys. **134**, 024113 (2010).
[53] H. Wang *et al.*, J. Phys. B **34**, 4417 (2001).
[54] O. Travnikova *et al.*, J. Electron Spectrosc. Relat. Phenom. **181**, 129 (2010).
[55] J. H. Callomon and F. Creutzberg, Philos. Trans. R. Soc., A **277**, 157 (1974).
[56] M. Meyer, A. Marquette, and M. Gisselbrecht, J. Electron Spectrosc. Relat. Phenom. **101–103**, 81 (1999).